Theory-guided growth of aluminum antimonide single crystals with optimal properties for radiation detection

Paul Erhart,[a] Daniel Åberg, Benjamin W. Sturm, Kuang-Jen Wu, and Vincenzo Lordi[b]
Lawrence Livermore National Laboratory, Livermore, California 94550, USA

(Received 27 August 2010; accepted 17 September 2010; published online 5 October 2010)

First-principles calculations are used to study the thermodynamic and electronic properties of a large set of intrinsic and extrinsic defects in AlSb. The results are employed in conjunction with experimental impurity data to devise an improved growth process for mitigating the detrimental effects of native defects and impurities. A codoping strategy using Te is demonstrated that leads to a significant increase in both mobility and resistivity without introducing lifetime-limiting deep levels. The resulting material exhibits an order of magnitude improvement in mobility-lifetime product and allows spectroscopic detection of α particles with AlSb. © *2010 American Institute of Physics*. [doi:10.1063/1.3499307]

Radiation detection plays an important role in a variety of fields ranging from x-ray medicine to detector design for synchrotron facilities to applications in homeland security. The current state-of-the-art material for room-temperature radiation detection[1] is $Cd_{1-x}Zn_xTe$ which has seen steady improvements over the past few years.[2] While this progress is encouraging, it is an important and necessary task to search for alternative materials both with regard to improving efficiency and reducing cost.

A radiation photon interacting with a semiconductor creates electron-hole (*e-h*) pairs that can be detected as an electric current by applying an external electric field. For high energy resolution, one needs to be able to accurately count the number of *e-h* pairs, which is proportional to the energy of the incoming photon. Any uncertainty in the magnitude of the signal current due to loss or gain of carriers between the absorption event and the collection of the induced current results in a degradation of the energy resolution of the detector. Candidate materials therefore need to possess the following properties: (i) large resistivity to minimize leakage currents, (ii) long carrier lifetimes, and (iii) high carrier mobilities to maximize the number of *e-h* pairs collected.

Given these criteria, finding new materials is a challenging task, particularly due to the apparently contradictory requirements of large band gap and high mobility. Experimental efforts in screening or optimizing materials are often limited by the difficulty in achieving the required purity to assess material performance, rendering an exclusively experimental approach time consuming and expensive. On the other hand, materials simulations and modeling are very helpful not only for selecting the most promising candidates but also for determining the ultimate limitations of a material, indicating optimal growth conditions, and identifying the best dopants and dopant concentrations. In this paper, we implement this approach and achieve an order of magnitude improvement in the properties of AlSb single-crystals.

We begin with a brief description of the properties of the initial AlSb samples. Then, by using the results of first-principles investigations of intrinsic[3] and extrinsic[4,5] point defects, we establish the theoretical limits of intrinsic net charge carrier concentrations and demonstrate how accidental impurity doping prevents reaching these values experimentally. We further demonstrate that C and O, which we find to be the most detrimental impurities in terms of carrier scattering, are also responsible for the experimentally observed *p*-type conductivity.[6] By screening several potential extrinsic donors, we predict Te to be the most suitable codopant and determine the doping concentration required for compensation. The properties of material grown according to these recommendations show a tremendous improvement, which enabled the spectroscopic detection of α-particle radiation using AlSb.

Bulk AlSb single-crystals were grown using the Czochralski method in a sealed system. The starting material consisted of pellets of 99.9999% pure Sb melted into a solid ingot in a quartz ampoule, and 99.9999% pure Al melted in a Al_2O_3 crucible. The molten Al is held for 24 h to outgas the oxide before introducing Sb into the melt. Single-crystal boules with diameters up to 13 cm were grown from a seed crystal pulled from the melt at ~ 1 cm/h while rotating at 2 rpm. Growth is performed at 1330 K, with heat provided by a graphite susceptor separated from the Al_2O_3 crucible by 1 atm continuous flow of Ar gas. Some samples were also subjected to postgrowth annealing at 1200 K under Sb overpressure for up to 8 days. We have achieved highly reproducible, large single crystal growths up to 900 g and ~ 20 cm^3 showing excellent uniformity and few, if any, macroscopic defects.

Dynamic secondary ion mass spectrometry was used to characterize the concentration of impurities in all samples. Electrical characterization of resistivity, majority carrier type, net carrier concentration, and mobility was performed with room temperature Hall measurements. Crystallinity of samples was confirmed with x-ray diffraction and Laue diffraction. Sample handling, including sawing and polishing in preparation for characterization, was performed in a glove box to minimize air exposure and prevent surface oxidation.

We have recently investigated the intrinsic point defects in AlSb within a density functional theory framework.[3] The aluminum vacancy (acceptor), the aluminum interstitial (donor), and the Sb_{Al} antisite (donor) were identified as the prevalent defects. Using the calculated defect formation energies we obtained equilibrium defect concentrations and

[a]Electronic mail: erhart1@llnl.gov.
[b]Electronic mail: lordi2@llnl.gov.

electron chemical potentials as a function of temperature. The intrinsic material was found to be weakly *n*-type—in contrast to experiment—with net charge carrier concentrations on the order of 10^{16}–10^{17} cm^{-3} near the growth temperature of 1330 K.

To understand the difference between the experimental data and the calculations for ideally pure AlSb, we computed the formation energies of common impurities as well as potential dopants from groups IV and VI of the periodic table.[7] We find that group IV elements energetically favor substitution on Sb sites and act as single acceptors. As the atomic number Z increases, the energetic difference between substitution on Sb and Al (which gives rise to donor defects) decreases. In the case of Sn this leads to equal formation energies for an electron chemical potential μ_e near the middle of the band gap and the possibility of forming Sn donors or Sn acceptors depending on growth and annealing conditions. Interstitial configurations do not play any role for group IV defects. Where a direct comparison is possible, the calculated defect transition levels are in good agreement with experiment.[4]

With the exception of oxygen, group VI elements show an energetic preference to substitute for Sb as well but unlike group IV elements, act as donors. For oxygen there are three configurations with similar formation energies. For μ_e in the upper two-thirds of the band gap, oxygen interstitials which act as acceptors dominate. For μ_e near the valence band edge and under Al-rich conditions, the substitution for Sb is energetically preferred with amphoteric characteristics. Finally, for μ_e near the valence band edge and under Sb-rich conditions, the O_{Sb}–Sb_{Al} donor complex is the most stable.

The absolute values of the formation energies show a systematic dependence on the atomic number Z. The formation energy decreases with Z for group IV elements, while the opposite is true for group VI elements. The lowest absolute formation energy is observed for oxygen, which indicates the risk for oxidation. Even for carbon, which shows the largest formation energies, the value is comparably low, about 1 eV, indicating that all of these elements can be relatively easily incorporated during growth, both accidentally and intentionally.

We can now combine the data for both the intrinsic and extrinsic defects to calculate defect concentrations and net charge carrier concentrations. To this end, we employ the strategy described in Refs. 4 and 8. The key results of this investigation are summarized in Fig. 1, which shows the net charge carrier concentration as a function of the chemical environment, for various doping conditions and at both the growth temperature of 1300 K and the annealing temperature of 1200 K. As discussed above, the intrinsic material is predicted to show *n*-type conduction with net carrier concentrations on the order of 10^{16}–10^{17} cm^{-3} at 1300 K. Comparison of the data obtained with and without band gap corrections [curves (a) and (b) in Fig. 1] shows only small differences. It is therefore justified to carry out the following analysis including impurities using the data *without* band gap corrections. Our baseline material is represented by curve (c) in Fig. 1, which includes carbon and oxygen at the experimentally observed impurity levels and which indeed predicts the "impure" as-grown material to be *p*-type in agreement with experiment.

The next step in our analysis is to consider the effect of native defects and impurities on the charge carrier mobilities.

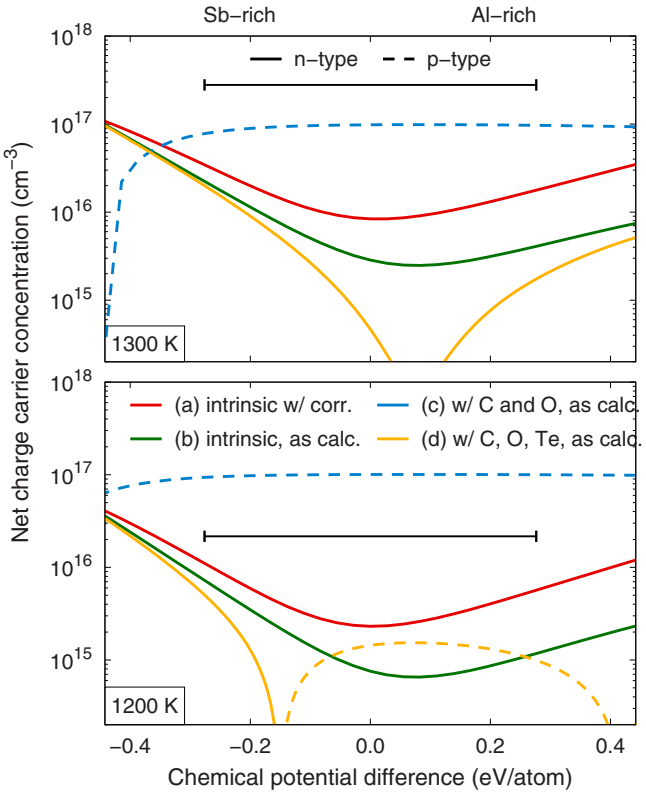

FIG. 1. (Color online) Net charge carrier concentrations at 1200 and 1300 K predicted by our thermodynamic analysis using first-principles data. (a) Intrinsic material using band gap corrections as described in Ref. 3; (b) intrinsic material using the as-calculated formation energies; (c) same as (b) but including C and O impurities with [C]=10^{17} cm^{-3} and [O]=10^{15} cm^{-3}; (d) same as (c) but including Te as a compensating dopant with [Te]=10^{17} cm^{-3}. Solid and dashed lines indicate net excess electrons (*n*-type) or holes (*p*-type), respectively.

Within first-order perturbation theory, the carrier scattering rate of a defect is determined by matrix elements of the scattering potential V_{sc}, which is given by the difference between $V_{\mathrm{def}}(\boldsymbol{r})$, the self-consistent potential in a cell containing the (relaxed) defect, and $V_{\mathrm{id}}(\boldsymbol{r})$, the potential in the ideal (defect-free) cell. Applying this approach to several impurities in AlSb,[10] we have shown that a very convenient measure for the *relative* carrier scattering rate of a defect is given by

$$\tilde{M}^2 = \left[\int |\nabla V_{sc}(\boldsymbol{r})| d\boldsymbol{r} \right]^2. \quad (1)$$

Since this expression can be evaluated much faster than a full scattering analysis, it is suitable for comparing a large number of defects and has thus been used in the present study. The results in Fig. 2 show that C and O are much stronger scatterers than any of the intrinsic defects, which explains their detrimental effects on the mobility. For both group IV and group VI elements, the relative scattering rates strongly decrease with Z, which can be attributed to the reduction in local strain with decreasing size mismatch between the impurity and Sb, resulting in a decrease in V_{sc}.

Based on these results, it is obvious that the incorporation of O and C must be suppressed to minimize their negative effect on carrier mobility. At the same time extrinsic donors need to be incorporated to achieve charge compensation of the as-grown *p*-type material and maximize resistivity. Based on Fig. 2, Te, which is most likely to substitute for Sb, is identified as the most promising candidate due to its

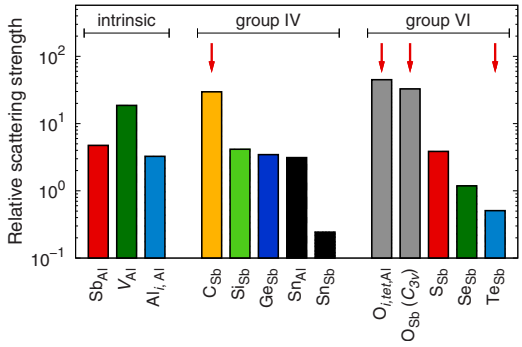

FIG. 2. (Color online) Relative scattering rates $\tilde{M}^2$ as defined in Eq. (1) for the most important intrinsic and extrinsic defects in AlSb. The data shown correspond to the most stable charge state of the respective defect.

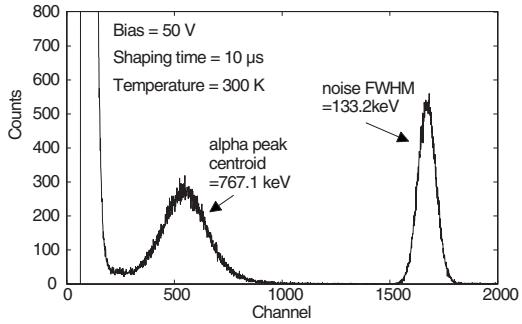

FIG. 3. α-spectrum from ^{210}Po acquired at room temperature with Te-doped AlSb single crystals. Incomplete charge collection has shifted the 5.3 MeV ^{210}Po α peak to 767.1 keV.

very small relative scattering rate. A further investigation of the electronic structure of Te also shows that it does not introduce deep states that could cause recombination and/or trapping and thereby limit carrier lifetimes.

By incorporating Te into our defect model, we are able to determine the concentration at which compensation is achieved as approximately 10^{17} cm^{-3}. Curve (d) in Fig. 1 shows that this concentration leads to a pronounced decrease in the net charge carrier concentration, and accordingly an increase in resistivity compared to case (c). Since this level of compensation is also comparable to the concentration of native defects (Sb_{Al}, $Al_{i,Al}$, V_{Al}) at this temperature,[3] which have significantly higher scattering rates, the introduction of the Te codopant has only minimal effect on mobilities.

Using the information from our first-principles defect model, we modified the growth process and dramatically improved the properties of AlSb bulk single crystals. We introduced 3% H_2 gas into the growth chamber to reduce oxidation and switched to an Al_2O_3 ampoule for melting Sb to further prevent incorporation of mobility-reducing O impurities into the material. Tellurium was incorporated at a concentration of 10^{17} cm^{-3} for carrier compensation. Without these modifications, our best material achieved a resistivity of up to 10^5 Ω cm with net charge carrier concentrations as low as 10^{13} cm^{-3}, but a mobility of only $\sim$10 cm^2/V s. Using the modified process but without Te doping, high mobilities of up to 400–500 cm^2/V s were achieved owing to the elimination of O scattering centers. Net carrier concentrations were, however, in excess of 10^{15} cm^{-3} and resistivities were low at $\sim$10–100 Ω cm. With the introduction of Te, we achieved a resistivity of $\sim 10^5$ Ω cm, a mobility in the range of 150–300 cm^2/V s, and net charge carrier concentrations below 10^{12} cm^{-3}.

The Te-doped material was fabricated into devices which showed high signal-to-noise ratios in α-spectra from a ^{210}Po source around 5.3 MeV as shown in Fig. 3. The devices consisted of $1\times1\times0.15$ cm^3 polished crystals with a Au guard ring electrode structure on the front and In–Ga liquid paint as back electrode. Determination of the electron drift figure of merit $\mu_e\tau_e$ was performed by measuring the shift of the α-spectrum peak centroid as a function of bias voltage and fitting the data to the Hecht relation.[11] The value of $\mu_e\tau_e=0.58\pm0.23\times10^{-4}$ cm^2/V for the undoped sample improved to $1.27\pm0.63\times10^{-4}$ cm^2/V by Te doping.

In summary, in this paper we have described a collaborative effort between experiment and theory that has led to an order of magnitude improvement in the properties of AlSb single crystals for radiation detection. Using first-principles calculations, we studied the thermodynamic and electronic properties of intrinsic and extrinsic defects, determined charge carrier types and concentrations, and obtained relative carrier scattering rates. We then devised a codoping strategy that enabled significant simultaneous improvement in both mobility and resistivity. Our results demonstrate the use of extremely low scattering codopants to achieve high resistivity and high mobility simultaneously, without introducing deep carrier lifetime-limiting states.

This work was performed under the auspices of the U.S. Department of Energy by Lawrence Livermore National Laboratory under Contract No. DE-AC52-07NA27344. The authors acknowledge support from the National Nuclear Security Administration Office of Nonproliferation Research and Development (NA-22) and the LLNL LDRD Program.

[1] A. Owens, J. Synchrotron Radiat. **13**, 143 (2006); G. A. Armantrout, S. P. Swierkowski, J. W. Sherohman, and J. H. Lee, IEEE Trans. Nucl. Sci. **N5–24**, 121 (1977).
[2] O. Limousin, Nucl. Instrum. Methods Phys. Res. A **504**, 24 (2003), and references therein; T. E. Schlesinger, J. E. Toney, H. Yoon, E. Y. Lee, B. A. Brunett, L. Franks, and R. B. James, Mater. Sci. Eng. R. **32**, 103 (2001); T. Takahashi and S. Watanabe, IEEE Trans. Nucl. Sci. **48**, 950 (2001); A. Kargar, A. M. Jones, W. J. McNeil, M. J. Harrison, and D. S. McGregor, Nucl. Instrum. Methods Phys. Res. A **558**, 497 (2006); P. N. Luke and E. E. Eissler, IEEE Trans. Nucl. Sci. **43**, 1481 (1996).
[3] D. Åberg, P. Erhart, A. J. Williamson, and V. Lordi, Phys. Rev. B **77**, 165206 (2008).
[4] P. Erhart, D. Åberg, and V. Lordi, Phys. Rev. B **81**, 195216 (2010).
[5] M.-H. Du, Phys. Rev. B **79**, 045207 (2009).
[6] M. D. McCluskey, E. E. Haller, and P. Becla, Phys. Rev. B **65**, 045201 (2001).
[7] Calculations were carried out within the local density approximation of density functional theory using the projector-augmented wave method (Ref. 12) as implemented in the Vienna ab initio simulation package (Ref. 13). We used 64-atom cells and a shifted $6\times6\times6$ Monkhorst–Pack mesh for Brillouin zone integrations. Monopole-monopole corrections were applied. The ionic positions were relaxed until the residual forces were below 30 meV/atom. The error in the formation energies due to finite-size effects can be estimated to be on the order of 0.1 eV (Ref. 3). More details on our calculations can be found in Refs. 3 and 4.
[8] P. Erhart and K. Albe, J. Appl. Phys. **104**, 044315 (2008).
[9] See Refs. 3 and 4 for a discussion of band gap corrections.
[10] V. Lordi, P. Erhart, and D. Åberg, Phys. Rev. B **81**, 235204 (2010).
[11] K. Hecht, Z. Phys. **77**, 235 (1932).
[12] P. E. Blöchl, Phys. Rev. B **50**, 17953 (1994); G. Kresse and D. Joubert, *ibid.* **59**, 1758 (1999).
[13] G. Kresse and J. Hafner, Phys. Rev. B **47**, 558 (1993); Phys. Rev. B **49**, 14251 (1994); G. Kresse and J. Furthmüller, Phys. Rev. B **54**, 11169 (1996); Comput. Mater. Sci. **6**, 15 (1996).